Carbohydrate Polymers 80 (2010) 53–64

Contents lists available at ScienceDirect

Carbohydrate Polymers

journal homepage: www.elsevier.com/locate/carbpol

Preparation of spherulites from amylose–palmitic acid complexes

Rajesh G. Bhosale, Gregory R. Ziegler *

Department of Food Science, Penn State University, 341 Food Science Building, University Park, PA 16802, United States

ARTICLE INFO

Article history:
Received 17 September 2009
Received in revised form 27 October 2009
Accepted 28 October 2009
Available online 3 November 2009

Keywords:
Amylose
Inclusion complex
Spherulite

ABSTRACT

We conducted a systematic study of the formation of spherulites from amylose–palmitic acid complexes. The independent variables included final heating temperature, intermediate quench temperature, final quench temperature and cooling rates. Spherulites were characterized by different techniques: optical microscopy, scanning electron microscopy, differential scanning calorimetry, X-ray diffraction, transmission electron microscopy and resistant starch content. Three distinct types of spherulite morphology were observed: spherical, sintered ("snowball") and torus/disc shaped. Spherical-shaped particles were formed at higher endpoint heating temperatures and exhibited mixed B+V-type XRD patterns. Torus-shaped spherulites formed from samples heated to 140 °C followed by slow cooling, and exhibited V-6_I type XRD patterns. Resistant starch estimated for spherulites formed by heating to 180 °C followed by cooling to 40 °C at 1 °C/min vs. those formed by heating to 140 °C, cooled to 90 °C at 1 °C/min then to 40 °C at 0.04 °C/min was 28% and 39%, respectively. Morphology of the amylose–PA spherulites after resistant starch determination for spherical spherulite shows distinct pores and uneven surface texture. In contrast, the torus-shaped spherulites were degraded with evidence of recrystallization.

1. Introduction

In a series of papers in this journal, Fanta and co-workers have reported on the formation of spherulites from starch–lipid inclusion complexes (Byars, Fanta, & Felker, 2003, 2006; Fanta, Felker, Shogren, & Salch, 2006, 2008; Fanta, Felker, Shogren, Byars, & Salch, 2005; Fanta, Felker, & Shogren, 2002; Fanta, Shogren, & Salch, 1999; Peterson, Fanta, Adlof, & Felker, 2005; Shogren, Fanta, & Felker, 2006). Spherulites were produced by the slow (≈0.04 °C/min) cooling of starch–lipid mixtures after steam-infusion "jet" cooking at 140 °C. The process resulted in the formation of spherulites of two morphologies – spherical/lobed and torus/disc – the proportion of which varied depending on the starch concentration, fatty acid used, the pH of the dispersion, the cooling rate and whether the dispersion was stirred during cooling. The spherical/lobed type were generally larger than the torus/disc type, and reportedly exhibited 7_I or mixed 6_I and 7_I V-type WAXS patterns, whereas the torus/disc type exhibited only the 6_I V-type pattern. The existence of crystals comprising 7-glucose monomers per turn has been questioned; this pattern may result from a 6_{III} complex with greater space between the helices (Conde-Petit, Escher, & Nuessli, 2006).

In the majority of cases, Fanta et al. allowed the cooked starch dispersions to cool at room temperature in either a 1 L or 6 L Dewar flask, with the result that the cooling rate was variable and uncontrolled (Fanta et al., 2008). In several cases (Byars et al., 2003, 2006), a rapid viscoanalyzer was used to control the cooling rate, but this method also involved mechanical shear. Fanta et al. (2008) have speculated that differences in spherulite morphology were caused by variation in cooling rates due to the different size Dewar flasks.

The focus of the body of work by Fanta et al. has been the jet-cooking process as a convenient and inexpensive method for producing starch-based compositions, but no explanation is given for the selection of the 140 °C cooking temperature. Sievert and Holm (1993) observed incomplete complexation when starch–lipid dispersions were heated to temperatures below 170 °C, so it is possible that the relatively low yield of spherulites as a percentage of starch (<60%, typically 20%) was due to incomplete complexation at sub-optimal cooking temperatures (Fanta et al., 2008).

Over the same period of time, we have studied the formation of starch spherulites in the absence (or relative absence) of lipid, formed by the rapid cooling of starch previously heated to temperatures in excess of ≈170 °C (Creek, Benesi, Runt, & Ziegler, 2007; Creek, Ziegler, & Runt, 2006; Nordmark & Ziegler, 2002a,2002b; Ziegler, Creek, & Runt, 2005; Ziegler, Nordmark, & Woodling, 2003). Unlike the work of Fanta et al., our approach has been to study this phenomenon on a laboratory scale using a differential scanning calorimeter to accurately control the thermal profile. In addition to the inherent nature of the starch polymers, it was the specifics of this thermal profile, especially the endpoint heating temperature, the cooling rate and the final quench temperature, that determined whether spherulites form and their resulting morphology.

* Corresponding author. Tel.: +1 814 863 2960; fax: +1 814 863 6132.
E-mail address: grz1@psu.edu (G.R. Ziegler).

0144-8617/$ - see front matter © 2009 Elsevier Ltd. All rights reserved.
doi:10.1016/j.carbpol.2009.10.069

Spherulitic morphology has also been reported for inclusion complexes between amylose and a number of flavor compounds (Conde-Petit et al., 2006; Heinemann, Escher, & Conde-Petit, 2003). Morphology was kinetically determined, but contrary to lipid-free systems (Creek et al., 2006, 2007) spherulites were favored at slow cooling rates and gel networks favored under conditions of rapid aggregation.

With this in mind, we undertook a systematic investigation of spherulite formation from starch–palmitic acid mixtures under controlled conditions, with the intention of more clearly understanding the conditions that favor spherulite formation, determine spherulite morphology, and result in high yields. As with previous studies we have used amylose to avoid the complicating factor of starch branching.

2. Materials and methods

2.1. Materials

Potato amylose ($\overline{DP} = 900$, essentially free of amylopectin) was purchased from Sigma–Aldrich Co. (Milwaukee, WI). Palmitic acid (>95%) was obtained from (Eastman Kodak Company, Rochester, NY). Deionized water was used in the preparation of the starch suspensions. All chemicals used for transmission electron microscopy were of microscopy grade. Copper grids for TEM were purchased from Electron Microscopy Sciences (Fort Washington, PA). Eponate resin was purchased from Ted Pella (Redding, CA). The resistant starch assay kit (K-RSTAR) that included thermostable α-amylase and amyloglucosidase was purchased from Megazyme International Ireland Ltd. (Wicklow, Ireland).

2.2. Methods

2.2.1. Preparation of amylose–palmitic acid spherulites

Palmitic acid (5% weight basis of amylose) was dissolved in a minimum amount of ethanol and the solution intimately mixed with the starch. The ethanol was allowed to evaporate under ambient conditions. The amylose–palmitic acid mixture (4–6 mg) was diluted to 10% w/w in deionized water and hermitically sealed in high-volume (60 μl) stainless steel differential scanning calorimeter (DSC) pans (Perkin–Elmer Instruments, Norwalk, CT). After 12 h, samples were subjected to different thermal treatments as per the experimental design (Table. 1) in either a Pyris 1 or Pyris 7 DSC (Perkin–Elmer Instruments, Norwalk, CT). They were held in the calorimeter at their quench temperatures for 24 h before analyses by microscopy or DSC. Calorimeters were calibrated with indium, and an empty stainless steel pan was used as the reference during all heating and cooling procedures. Re-scans were performed from 20 to 180 °C at heating rate of 10 °C/min. The Pyris software was used to calculate transition temperatures (°C) and enthalpy (J/g).

Table 1
Experimental design.

Experiment	T_m (°C)	Rate 1 (°C/min)	T_{inter} (°C)	Rate 2 (°C/min)	T_f (°C)
1[a]	140	50	90	1	40
2	180	1	70	0.04	10
3	180	1	90	1	40
4	140	50	70	0.04	10
5	180	50	70	1	40
6	140	1	90	0.04	10
7	180	50	90	0.04	40
8	140	1	70	1	10
9	180	50	90	1	10
10	140	1	70	0.04	40
11	160	25.5	80	0.52	25
12[b]	140	50	90	0.04	40

Where T_m is the maximum heating temperature, T_{inter} and T_f are intermediate and final cooling temperature. The initial temperature and heating rate were 40 °C and 50 °C/min, respectively.

[a] Also run with a 30 min hold at 90 °C.

[b] Thermal process most like that of Fanta et al. (2008).

2.2.2. Optical microscopy

Spherulites prepared by Section 2.2.1 were removed from the DSC pans using a laboratory spatula, dispersed in a drop of deionized water, mounted on Fischer Brand frosted (pre-cleaned) microscope slides including a coverslip (Fisher Scientific, Pittsburgh, PA) and viewed with an Olympus BX 41 microscope equipped with a SPOT Insight QE camera (Hitech Instruments, Edgemont, PA). Photomicrographs were recorded using SPOT analytical and controlling software (SPOT Diagnostic Instruments, Sterling Heights, MI).

2.2.3. Scanning electron microscopy (SEM)

A small amount of spherulite sample was dispersed in ethanol and then filtered through a 13 mm circular polycarbonate membrane of 1 μm pore size (GE Water & Process Technologies, Trevose, PA) to uniformly deposit spherulites on the membrane without agglomeration. This membrane was applied to specimen stubs with double sticky conductive carbon adhesive tape. The samples were sputter-coated with 10 nm Au/Pd (BAL-TEC SCD 050; US-TechnoTrade, Manchester, NH), and examined using an environmental scanning electron microscope (FEI Quanta 3100 ESEM, FEI Company, Hillsboro, OR) at an accelerating voltage of 20 kV and a chamber pressure of 0.68 Torr.

2.2.4. Hot-stage microscopy

An optical pressure cell, constructed from an HPLC UV–vis detector, was utilized in conjunction with a Linkham LTS 350 hot stage and LinkSys 32 temperature control and data acquisition software (Linkam Scientific Instruments, Surrey, UK) to visualize the processes of spherulite melting/dissolution. Spherulites were observed using the optical microscope described above while heating from 30 to 160 °C. Actual temperature of the sample was measured using a thermocouple within the sample volume.

2.2.5. Transmission electron microscopy

To a small amount of spherulite sample in a microcentrifuge tube 0.5 ml of 1% periodic acid solution was added and allowed to react for 30 min, after which the samples were washed three times with deionized water. The sample was stored in saturated semithiocarbazide (0.5 ml) for 24 h. The semithiocarbazide solution was removed and a 1% silver nitrate solution was added as per Gallant, Mercier, and Guilbot (1972). Samples were stored with silver nitrate for 4 d, after which they were washed three times with deionized water. Samples were dehydrated by ethanol–acetone: 50% ethanol, 70% ethanol, 90% ethanol, twice with 100% ethanol, three times with electron microscopy grade 100% ethanol, and three times with acetone (each step consisting of 5 min). Samples were then infiltrated with increasing concentration of eponate resin: 50% eponate resin in acetone for 5–6 h, 75% eponate resin in acetone overnight, 100% eponate resin for 5 h, and a further exchange of 100% eponate resin prior to polymerization at 70 °C overnight. Ultrathin sections (60–90 nm) of embedded samples were obtained using an LKBIII 8800 Ultramicrotome (Leica, Dearfield, IL) and collected on copper grids. Samples were examined using a transmission electron microscope (Model 1200EXII, JEOL, Peabody, MA) at an accelerating voltage of 80 kV. Images that were collected were chosen to be representative of the total population of spherulites.

2.2.6. X-ray diffraction

A subset of samples was chosen for X-ray diffraction analysis. For treatment 4, the contents of four replicate DSC pans were pooled, washed twice with 50% ethanol–water solution, dispersed in a minimum amount of 100% ethanol and dried at 40 °C in a hot air oven. To obtain enough sample for both XRD and resistant starch determination, samples for treatment 3 and 6 were prepared in a 3 ml high-pressure stainless steel micro-reactor (MS – 2, High Pressure Equipment Company, Erie, PA). For treatment 3, the sample was heated in a laboratory convection oven (VWR International, Bristol, CT) from 40 @180 °C at rate of ≈30 °C/min, and then cooled stepwise at the rate of 10 °C/10 min from 180 @40 °C. Similarly for treatment 6, the sample was heated from 40 @140 °C at the rate of ≈30 °C/min, and then first cooled stepwise to 90 °C at the rate of 10 °C/10 min, then from 90 @40 °C at the rate of 2.5 °C/h. Both samples were washed twice with 50% ethanol–water solution, dispersed in 100% ethanol and dried in a hot air oven at 40 °C. Their morphologies were observed using optical microscopy and found to be the same as those of the spherulites prepared by DSC.

X-ray diffraction was carried out on a Rigaku MiniFlex II Desktop X-ray powder diffractometer (Rigaku Americas Corp., The Woodlands, TX). The operating conditions were Cu Kα1 radiation (0.154 nm), voltage 30 kV and current 15 mA. Approximately 100 mg of sample powders (equilibrated to a relative humidity of 0.85 at 20 °C) were loaded onto a glass plate in the form of a thin disk made by lightly compressing the powder using an IR pellet maker, and scanned over the range 5–30° Bragg angles at the rate of 1°/min in steps of 0.02°.

2.2.7. Estimation of resistant starch (RS)

Samples for treatment 3 and 6 made in the micro-reactor (Section 2.2.6) were used for resistant starch determination. The official method (AOAC Method 2002.02, AACC Method 32–40) for in vitro RS determination was used (McCleary, McNally, & Rossiter, 2002). Approximately 100 mg starch was weighed into 50 ml polypropylene bottles and 4 ml of enzyme buffer (10 mg/ml pancreatic α-amylase with 10 μl/ml diluted amyloglucosidase (3 U/ml) in 0.1 M, pH 6 sodium malate buffer containing 0.3 g/l $CaCl_2$ and 0.2 g/l NaN_3) was added to the sample. The sample was vortexed and immediately placed into a shaking water-bath (200 strokes/min) at 37 °C. After 16 h of digestion, the tube was removed from the water-bath and 4 ml of ethanol was added. The tube was vortexed and centrifuged at 1500*g* for 10 min. The supernatant was removed and the precipitate washed with 4 ml of 50% ethanol (v/v). The tube was centrifuged again at 1500*g* for 10 min. The supernatant was decanted and the washing step was repeated once more. The supernatant was carefully removed. The pellet was resuspended in 2 ml of 2 M potassium hydroxide with stirring for 20 min in an ice/water-bath. Sodium acetate buffer (8 ml of 1.2 M, pH 3.8) was added to each tube with stirring. Immediately a 0.1 ml aliquot of amyloglucosidase (3300 U/ml) was added and the tube placed in a water-bath at 50 °C for 30 min with constant agitation. The contents of the tubes were quantitatively transferred to volumetric flasks. After volume adjustment with deionized water a 0.1 ml aliquot was added to small test tubes containing 3 ml of GODOP reagent (glucose oxidase >12,000 U/l, peroxidase >650 U/l, 4-aminoantipyrine 0.4 mM) and incubated at 50 °C for 20 min. The absorbance of the samples was read at 510 nm against a reagent blank and compared to the glucose standard supplied with the kit. The resistant starch (RS) was calculated as:

$$\text{Resistant Starch (g/100 g sample)(samples containing} > 10\%\ \text{RS)} = \Delta E \times F \times 100/0.1 \times 1/1000 \times 100/W \times 162/180 = \Delta E \times F/W \times 90$$

where ΔE = absorbance (reaction) read against the reagent blank, F = conversion from absorbance to micrograms (the absorbance obtained for 100 μg of glucose in the GOPOD reaction is determined and F = 100 (μg of glucose) divided by the GOPOD absorbance for this 100 μg of glucose), 100/0.1 = volume correction (0.1 ml taken from 100 ml), 1/1000 = conversion from micrograms to milligrams, W = dry weight of sample analyzed = "as is" weight × (100-moisture content)/100, 100/W = factor to present RS as a percentage of sample weight, and 162/180 = factor to convert from free glucose, as determined, to anhydro-glucose as occurs in starch.

3. Results and discussion

The experimental conditions were chosen based on the reports of Fanta et al. (2008), i.e. steam jet-cooking at 140 °C, followed by rapid cooling to 90 °C, then slow cooling to 40 °C, our own experience, i.e. heating to 180 °C followed by rapid cooling to a temperature below 70 °C (e.g. Creek et al., 2006), and that of Sievert and Holm (1993) for maximum complexation observed at temperatures above 170 °C. A fractional factorial design, with two levels, five factors (maximum heating temperature, cooling rate 1, intermediate cooling temperature, cooling rate 2, and final cooling temperature), and a center point was created using EChip® (Hockessin, DE) experimental design software (Table 1).

3.1. Spherulite morphology

Spherulite formation was assessed using brightfield and polarized light microscopy (Fig. 1). Seven of 11 experimental treatments were successful in forming spherulites with varying yield. Consistent with the observations of Fanta et al. (2002) two distinct morphologies – spherical and torus/disc shaped – were observed. Treatments where T_{max} was 180 °C preferentially formed the spherical morphology, while those with T_{max} of 140 °C resulted in torus/disc morphology. Treatment 3 (T_{max} = 180 °C, T_{inter} = 90 °C, T_f = 40 °C, Rate 1 = Rate 2 = 1 °C/min) was unusual in that it resulted in a high yield of relatively large (15–25 μm) well-formed spherulites. Under the same conditions without added lipid, cooling at 1 °C/min yielded few spherulites of smaller size (10–15 μm) (Creek et al., 2006). Furthermore, the addition of L-α-lysophosphatidylcholine suppressed spherulite formation in amylose dispersions heated to 180 °C (Creek et al., 2007), while the addition of palmitic acid here did not. A sub-class of spherical particles comprising smaller sub-particles that appeared to be sintered together were termed "snowball" morphology and resulted from the most rapidly cooled samples.

While these results appear superficially similar to those of Fanta et al. (2008), it is possible that the larger spherical particles are fundamentally different. Fanta et al. (2002) reported that the larger fraction of spherocrystals demonstrated either a two- or four-lobed appearance, a 7_1 V-type XRD pattern, and a ringed birefringence when viewed between crossed polarizers. While some of the larger spherical particles observed in this study appear lobed (Fig. 1), they differed in their XRD pattern (see Section 3.3) and do not reveal a ringed birefringence when viewed between crossed polarizers.

Treatment 7 (180 → 90 → 40 °C @50–0.04 °C/min) produced highly agglomerated small particles of questionable spherulitic character (no obvious Maltese cross when viewed between crossed polarizers) that are similar to the cauliflower-shaped sub-fraction obtained by Fanta et al. (2008) on jet-cooking high-amylose starch and fatty acids.

Neither treatment 1 (140 → 90 → 40 °C @50–1.0 °C/min) nor treatment 4 (140 → 70 → 10 °C @50–0.04 °C/min) produced a significant number of spherulites. This suggested that it was not cooling rate *per se* that was the important parameter, but perhaps the

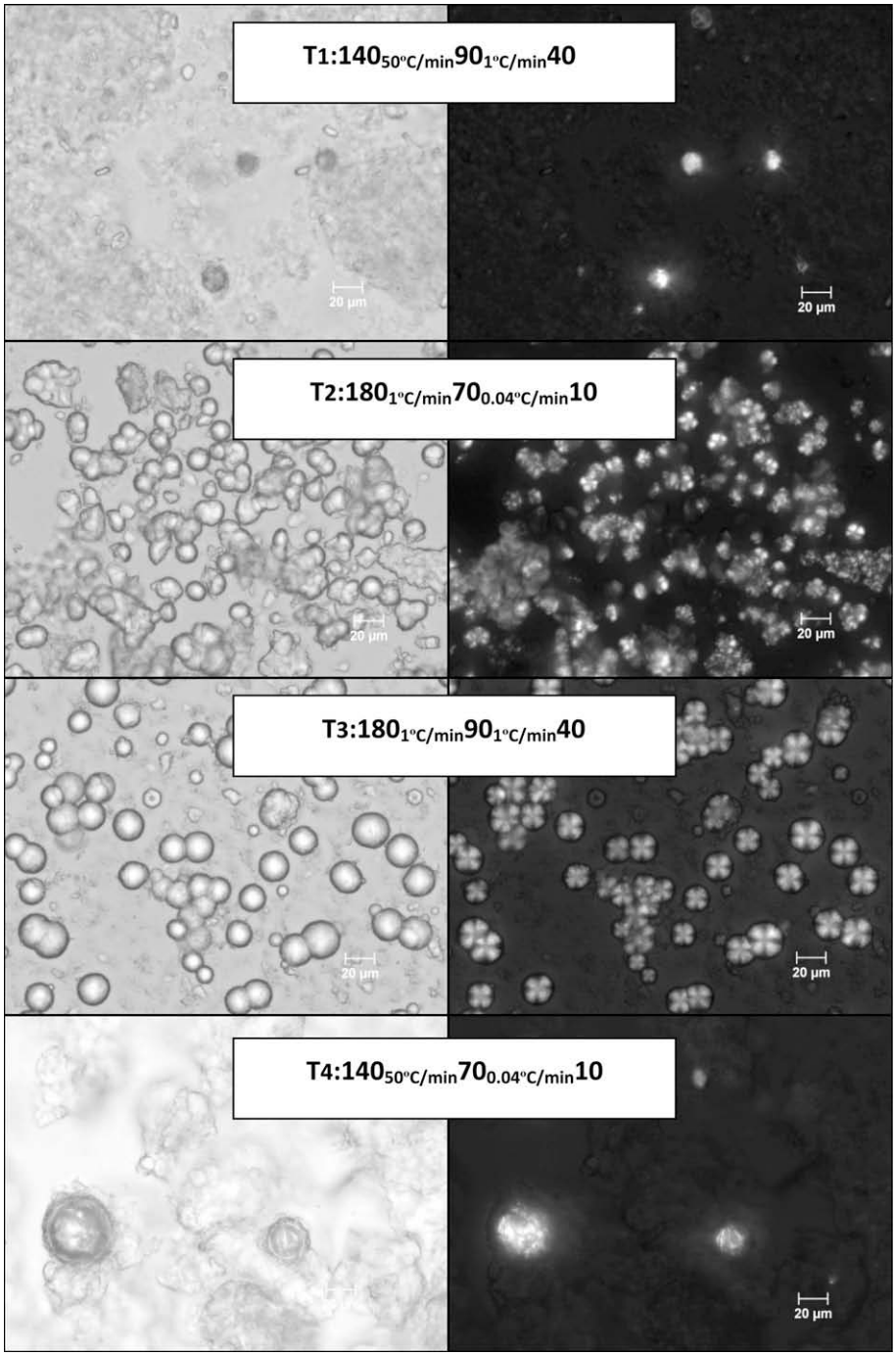

Fig. 1. Optical micrographs showing morphology of amylose–palmitic acid complexes. Brightfield illumination (left), between crossed polarizers (right). Bar equals 20 µm.

time above a critical temperature (say 80 °C) (Whittam et al., 1989). Therefore, we repeated treatment 1 adding a 30 min holding time at 90 °C, but the results were the same, with a few torus-shaped spherulites, a majority of gel-like character, and birefringent droplets of uncomplexed palmitic acid (Fig. 1: T1).

Large spherulites produced by treatment 3 (180 → 90 → 40 °C @1.0–1.0 °C/min) were well-formed with a fine surface texture that appeared to comprise fine crystalline fibrils (Fig. 2). By contrast, treatment 2 (180 → 70 → 10 °C @1.0–0.04 °C/min) produced spherulites with large cracks and fissures (Fig. 2). This may have resulted from the deeper quench for treatment 2 causing more rapid crystallization and the buildup of internal stresses. Treatments 5 (180 → 70 → 40 °C @50–1.0 °C/min) and 9 (180 → 90 → 10 °C @50–1.0 °C/min) with their rapid quench at high temperature formed rough spherulites that appeared to comprise smaller particles that were prone to aggregation (Fig. 2). Similar morphology was evident in the background of treatment 3 (Fig. 2) and has been observed by Fanta et al. (2008).

Treatments 6 (140 → 90 → 10 °C @1.0–0.04 °C/min), 8 (140 → 70 → 10 °C @1.0–1.0 °C/min) and 10 (140 → 70 → 40 °C @1.0–0.04 °C/min) all produced torus morphology. Treatment 6, which experienced a greater time at higher temperature, resulted in a more complete formation of relatively separate spherulites with little non-spherulitic material vis-à-vis treatments 8 and 10.

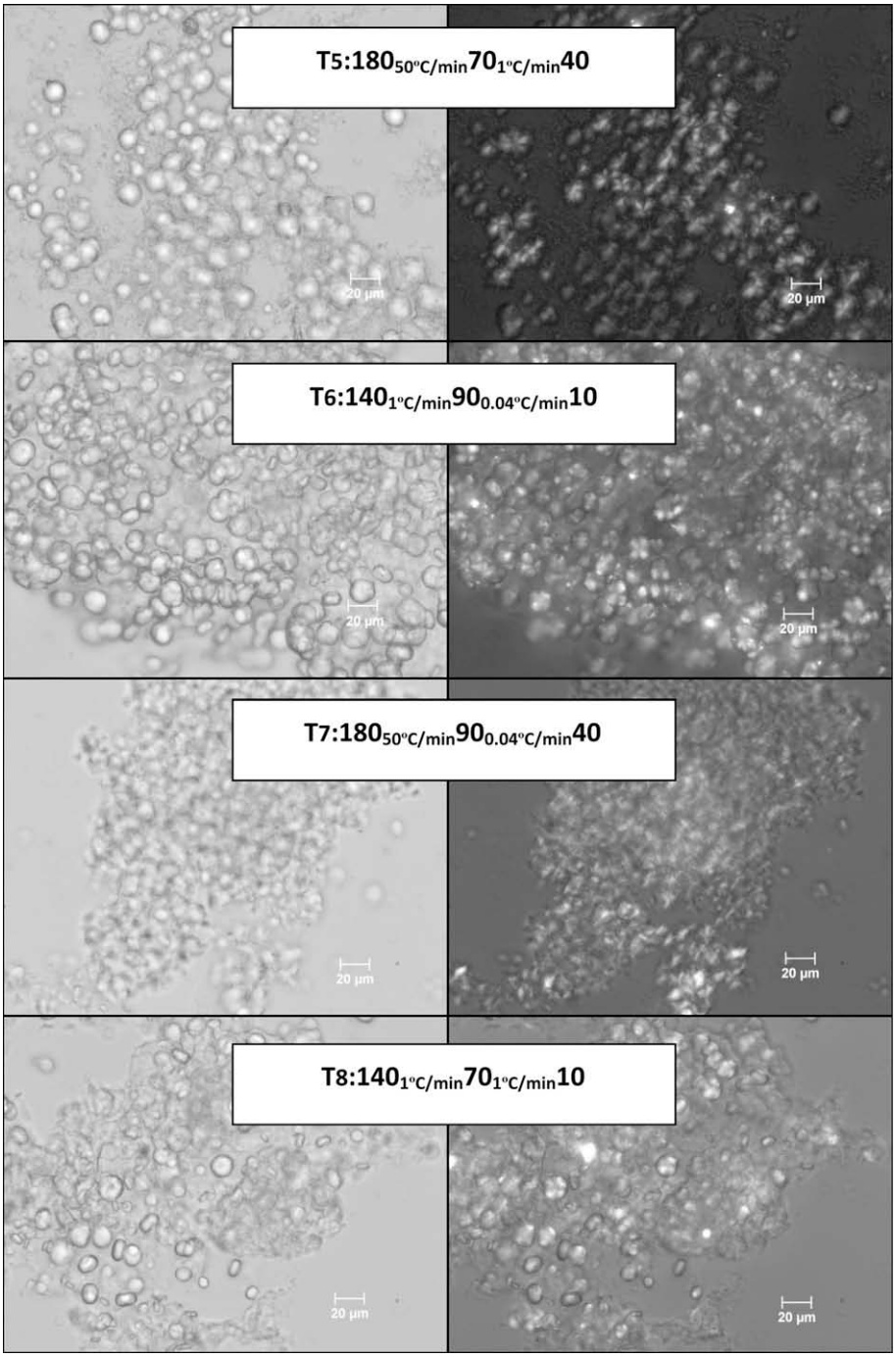

Fig. 1 (*continued*)

Treatment 12 (140 → 90 → 40 °C @50–0.04 °C/min), which most closely resembled the thermal profile of Fanta et al. (2008) without stirring, similarly resulted in the formation of torus-shaped spherulites. Felker and Fanta (2006) observed the formation of large spherical/lobed spherulites at higher temperature than smaller torus/disk shaped spherulites, while very small (<1 μm diameter) spherulites predominated on rapid cooling. It should be noted that the jet-cooking process employed by Fanta et al. results in a near instantaneous drop in temperature from 140 to ca 90 °C, which is accompanied by intense shear. Even so, similar morphology resulted from both processes.

3.2. Hot-stage microscopy

The melting/dissolution of spherulites was directly observed using hot-stage microscopy. A dispersion of spherulites in excess water was heated from 30 to 160 °C and the temperature where dissolution was visually observed noted. Torus-shaped spherulites from treatments 6, 8 and 10, were observed melting in a narrow range between 107 and 110 °C. Spherical-shaped spherulites, e.g. from treatment 3, melted over a broad range. A loss of birefringence was observed at about 116 °C, with final breakdown of the spherical structure occurring at 130 °C. Thermal behavior will be further discussed in Section 3.4.

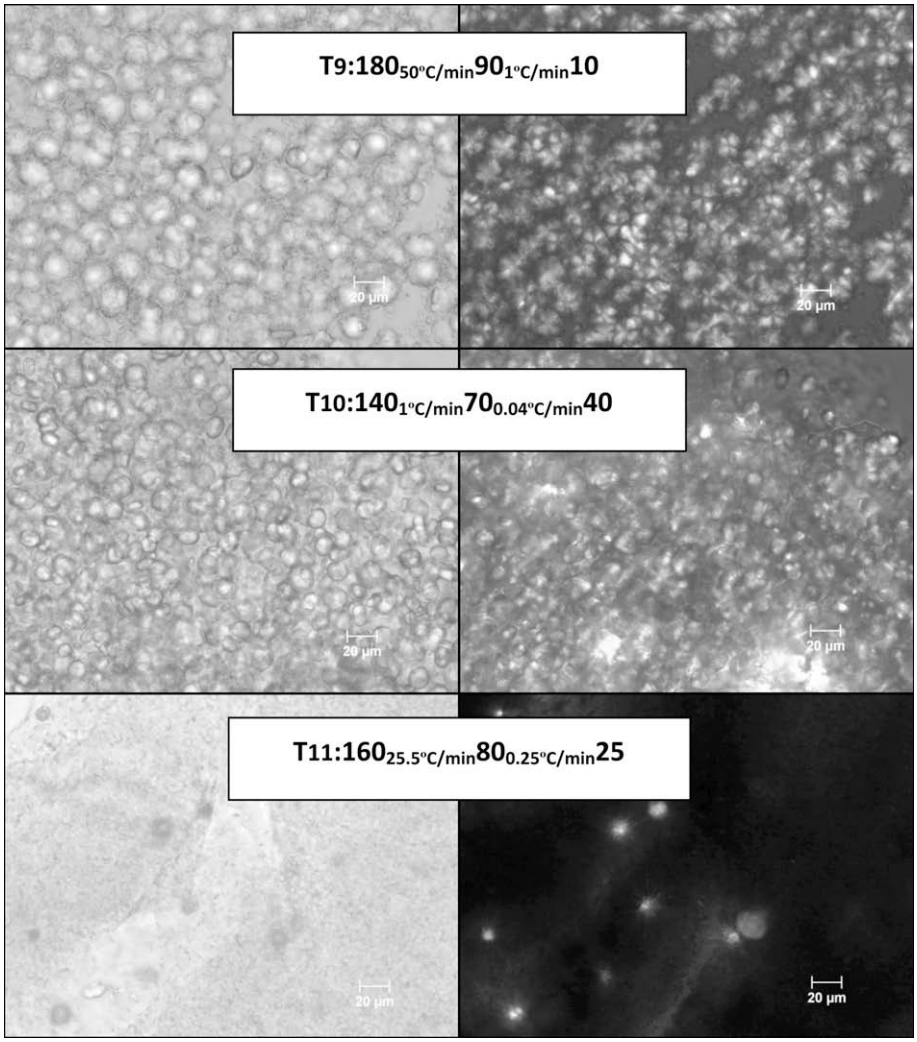

Fig. 1 (*continued*)

In a separate experiment, the formation of spherulites was observed using hot-stage microscopy. A 10% by weight mixture of amylose–PA (5% w PA/w amylose) in deionized water was heated from 40 to 140 °C in the optical pressure cell, then allowed to cool from 140 to 90 °C at rate of 1 °C/min. The sample was further cooled from 90 to 40 °C in 5 °C steps of 1 h each. Spherulite formation was initiated at a temperature of 82 °C in the torus form and further cooling to 40 °C led to an increase in torus size.

3.3. X-ray diffraction (XRD)

A larger sample size was required for powder X-ray diffraction, which was obtained by preparing samples in a 3 ml micro-reactor (treatments 3 and 6) or by pooling the contents of four DSC pans (treatment 4). We selected three samples for further analysis by XRD: spherical morphology (treatment 3), gel morphology (treatment 4) and torus morphology (treatment 6). Treatment 4 (140 → 70 → 10 °C @50–0.04 °C/min), with a rapid quench below 80 °C, demonstrated a mostly amorphous XRD pattern with very weak V-type tendency, i.e. a small peak at $2\theta = 20°$ (Fig. 3). Treatment 6 (140 → 90 → 10 °C @1.0–0.04 °C/min) revealed a characteristic V-6 diffraction pattern (Fig. 3).

Treatment 3 (180 → 90 → 40 °C @1.0–1.0 °C/min) resulted in a mixed B, V-type pattern (Fig. 3). Creek et al. (2007) observed complex formation between amylose and L-α-lysophosphatidylcholine to be exclusive of the formation of B-type crystallinity, and it was proposed that the kinetics of formation of the V-type single helix was faster than that of the purported B-type double helix. However, this does not seem to be the case with palmitic acid complexes. Perhaps the XRD pattern of treatment 3 resulted from the presence of two morphologies, the large well-formed spherulites and the smaller particulate morphology (visible in the background of Fig. 2), with differing XRD patterns.

3.4. Thermal behavior

Transition temperatures and their associated enthalpies are detailed in Table. 2. DSC thermograms for treatment 3, 4 and 6 are shown in Fig. 4. As expected, the thermograms were rather complex. Two or three major endotherms were commonly observed: the lowest at about 60 °C due to uncomplexed crystalline palmitic acid, 90–100 °C presumably for the type I amorphous amylose–fatty acid complex, and 100–120 °C for the type II crystalline amylose–fatty acid complex (Fanta et al., 2002; Karkalas, Ma, Morrison, & Pethrick, 1995). In addition, a small endothermic transition between 130 and 140 °C was sometimes observed, most notably in treatment 3, which likely corresponded to the melting of B-type crystallinity (see Section 3.3). Uncomplexed palmitic acid melted

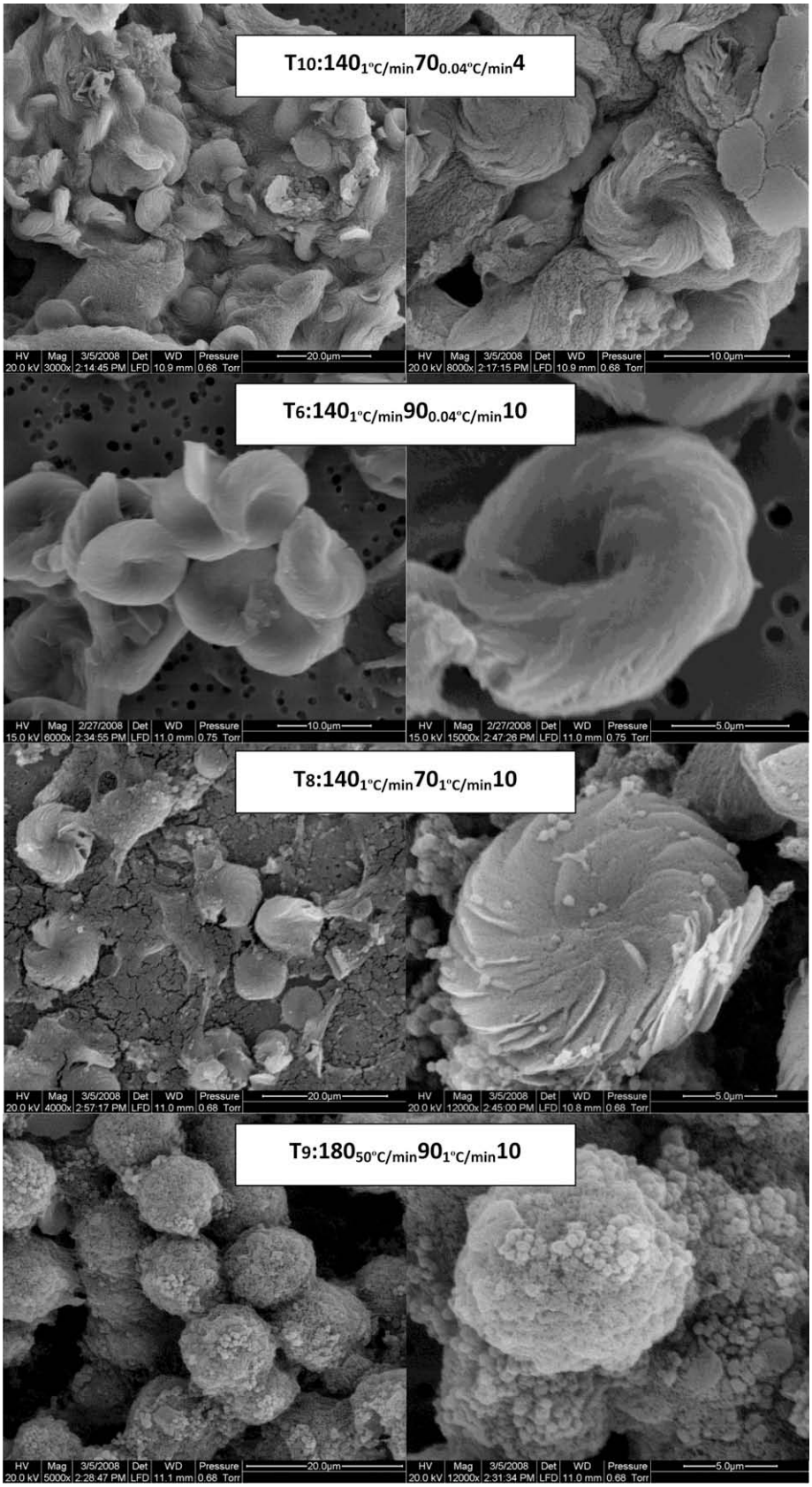

Fig. 2. SEM images of amylose–palmitic acid spherulites. Scale bar marked on image.

at 61 °C with an enthalpy of 195.85 J/g. The uncomplexed lipid content was determined based on the residual melting enthalpy (Godet, Bizot, & Buléon, 1995). The % of complexed palmitic acid was calculated as

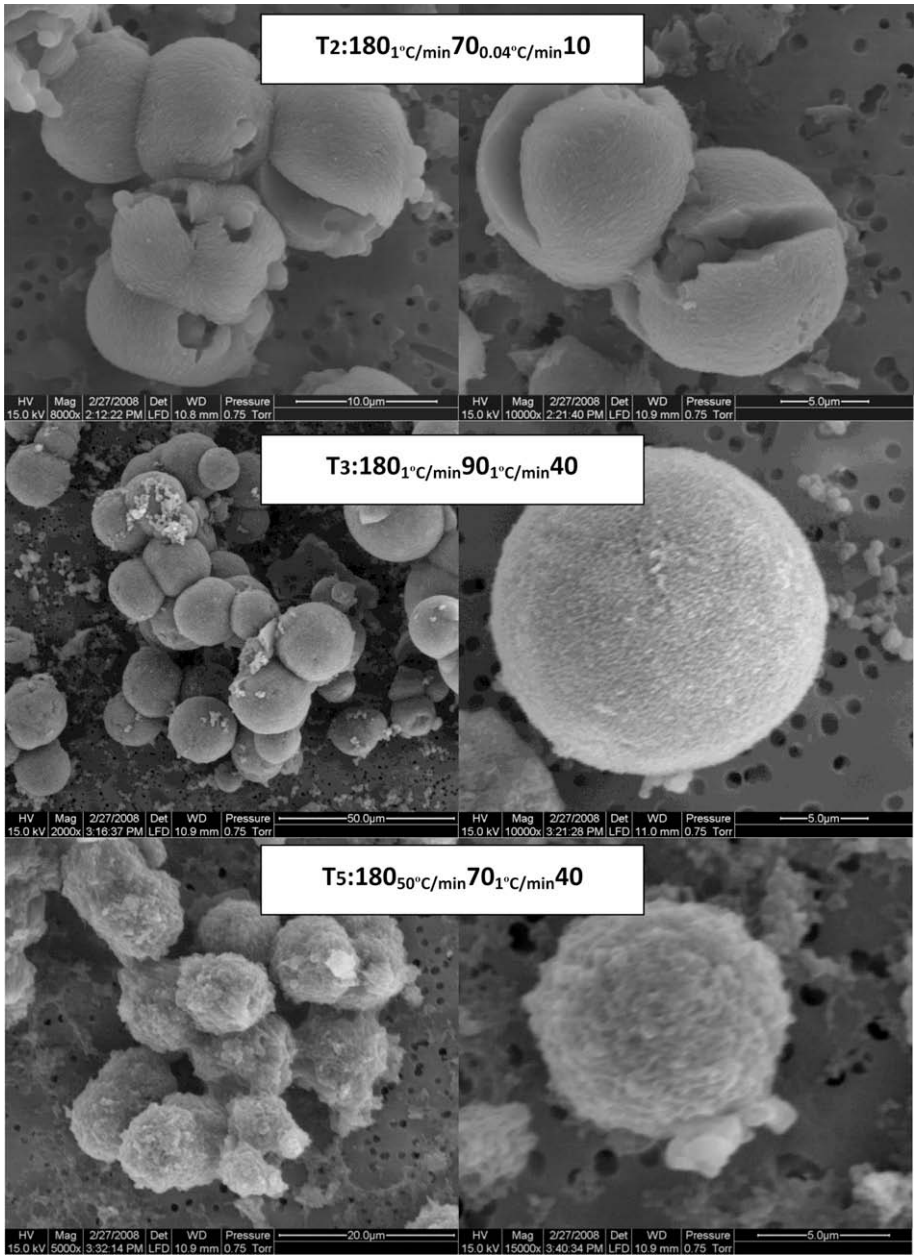

Fig. 2 (*continued*)

$$\left(1 - \frac{\Delta H_{\text{sample uncomplexed}}}{\Delta H_{\text{total uncomplexed}}}\right) \times 100$$

and varied from 22% (treatment 10) to 100% (treatment 6 and 12).

In general, deeper quenches or faster cooling rates resulted in lower percentages of complexation (compare treatments 6, 8 and 10). With shallower quenches and slower cooling rates (e.g. treatment 6) the crystalline complex had greater time to form resulting in complete complexation of the palmitic acid, relatively high melting temperature, and a high proportion of complex in the type II form. For treatment 6, spherulite melting was observed visually (Section 3.2) between 107 and 110 °C, coincident with the peak for type IIa complex observed by DSC (Fig. 4). The shape of the endotherm for treatment 6 in Fig. 4 suggests a recrystallization (or polymorphic transformation) occurring during the DSC measurement, with the result that a high percentage of type IIb complex is observed at a temperature exceeding that where the spherulites were seen to melt. Treatment 7 (180 → 90 → 40 @50–0.04) resulted in only 76% complexation, but a greater enthalpy than treatment 6 with 100% complexation. This is because for treatment 7, type IIb complex predominated and there was no polymorphic transformation observed; the exothermic nature of the transformation resulted in a lower total enthalpy for the endotherm in treatment 6 (140 → 90 → 10 @1.0–0.04). Such an annealing or recrystallization was suggested by Godet et al. (1995) and Karkalas et al. (1995).

For treatment 4 (140 → 70 → 10 @50–0.04), type I complex only was observed by DSC (Fig. 4). This is consistent with the largely amorphous XRD pattern (Fig. 3) and the deeper quenches, as complexation at low (<60 °C) temperatures results in little crystallographic order (Gelders et al., 2005). For treatment 3, a broad endotherm spanning the range from about 75 to 115 °C was observed (Fig. 4). Visually, large spherical spherulites seen in these samples lost their birefringence beginning coincident with the end of this endotherm (Section 3.2), while structural integrity was not lost until 130 °C, coincident with a high temperature endotherm tentatively assigned to the B-type crystallinity observed by XRD (Fig. 3).

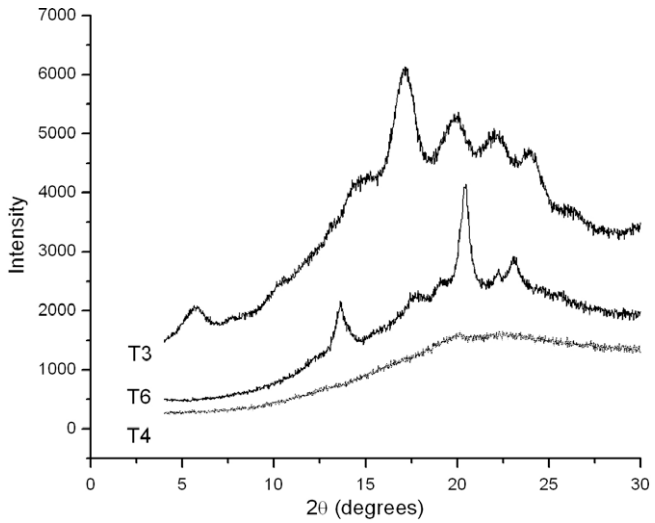

Fig. 3. X-ray diffraction diagrams of spherulites obtained from treatment 3, 4 and 6.

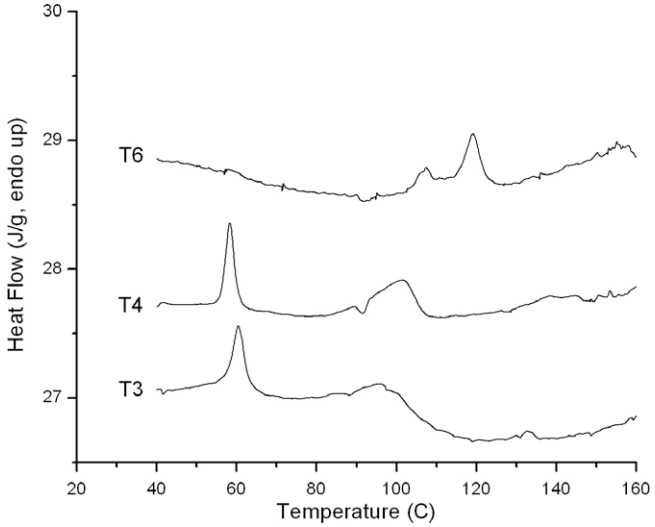

Fig. 4. DSC thermograms of spherulites obtained from treatment 3, 4 and 6.

While qualitatively consistent, the strong B-type reflections at approximately $2\theta = 5.5°$ and 17° seem disproportionate to the low enthalpy observed by DSC between 125 and 135 °C, and the V-type reflection at $2\theta = 20°$ appears more intense than might be expected of the type I amorphous complex. Furthermore, we have previously observed principally B-type crystallinity in spherulites melting in the range 60–100 °C (Nordmark & Ziegler, 2002a), so it seems possible that the broad endotherm for treatment 3 in Fig. 4 results from both B- and V-type melting.

Similarly, treatment 2 (180 → 70 → 10 @1.0–0.04) resulted in a broad bimodal endotherm spanning the range 90–120 °C with the highest melting enthalpy (13.32 J/g). Since only about 39% of the palmitic acid was complexed, it is unlikely that this is entirely due to V-amylose, and likely results from a significant B-type fraction. This high crystallinity is supported by the strong birefringence (Fig. 1) and is consistent with B-type spherulites formed in the absence of lipid (Creek et al., 2006).

3.5. Transmission electron microscopy

The PATA reagent reaction was performed on bulk samples before embedding in resin and was used to preferentially stain amorphous areas to be compared with the crystalline regions (Godet, Bouchet, Colonna, Gallant, & Buléon, 1996). TEM images of amylose–PA spherulites are shown in Fig. 5. Spherulites from treatment 3 and 6 displayed structures of apparent polycrystalline nature with organized lamellar regions. The thickness of the lamellae for spherulites from treatment 3 ranged from 80 to 100 nm, while for spherulites from treatment 6, lamellae thickness ranged between 5 and 10 nm consistent with the findings of Godet et al. (1996) for DP 900 – palmitic acid complexes. At 5 nm the lamellar thickness corresponds to 6¼ turns of the V-helix or 37.5 glucose residues. This would be just slightly larger than required to accommodate two palmitic acid molecules (≈32 nm), which would likely be oriented tail-to-tail with the carboxyl head group located near the surface of the lamellae (Biais, Le Bail, Robert, Pontoire, & Buleon, 2006).

TEM of non-spherulitic complex from treatment 4 shows two types of morphology, oval shapes (60–80 nm on the long side, 20–30 nm on the short side) and spherical shapes (<10 nm) loosely assembled in a gel-like network. This morphology is very similar to the TEM morphology for amylose and *n*-butanol complexes (Kim & Lim, 2009; Kim, Yoon, & Lim, 2009). No obvious lamellae are observed, consistent with the largely amorphous XRD pattern (Fig. 3).

Table. 2
Thermal analysis of amylose–PA mixtures.

Experiment	T_{PA} (°C)	ΔH_{PA} (J/g)	ΔH_{PA}≠PA (J/g)	T_I (°C)	ΔH_I (J/g)	T_{II} (°C)	ΔH_{II} (J/g)	PA complexed (%)
1	57.58	6.26	8.66	–	–	101.33, 116.08	2.34, 1.66	27.00
2	58.17	5.02	8.18	87.13, 95.67[b]	0.57	108.67	13.32	38.59
3	60.40	4.74	9.25	96.19	8.33	132.76[a]	0.31	48.75
4	58.33	4.47	9.27	89.71	0.49	101.61	6.16	51.70
5	58.08	3.55	9.04	–	–	102.00	4.13	60.66
6	–	–	9.99	–	–	107.33, 119.17	8.12	100.00
7	58.25	2.17	9.71	92.58	1.14	102.17, 117.08	0.38, 9.88	77.00
8	61.51	4.83	9.69	–	–	104.67, 120.37	1.28, 2.58	50.06
9	58.58	4.79	9.51	83.50	0.88	102.08, 117.17	2.40, 1.64	49.56
10	58.45	8.48	10.71	–	–	103.66, 120.37	1.13, 5.89	20.82
11	5.873	5.68	8.92	92.67, 97.05	6.05	117.42	2.87	36.28
12[c]	–	–	8.60	–	–	106.01, 119.41	0.78 5.64	100.00

Where T_{PA}, T_I and T_{II} are melting temperature of palmitic acid, amylose–PA complex type I (≈80–100 °C) and type II (≈100–125 °C). ΔH_{PA}, ΔH_{PA}≠, ΔH_I and ΔH_{II} are melting enthalpy for palmitic acid of sample, melting enthalpy of total uncomplexed PA of sample before complexation, amylose–PA complex type I and type II.

[a] This temperature exceeds that usually observed for type II complexes and likely results from B-type crystallinity (see Section 3.3).

[b] A broad endotherm spanning the temperature range for both the 95.67 and 108.67 °C peaks was observed and integrated as one.

[c] This treatment most closely matches the thermal profile used by Fanta et al. (2008).

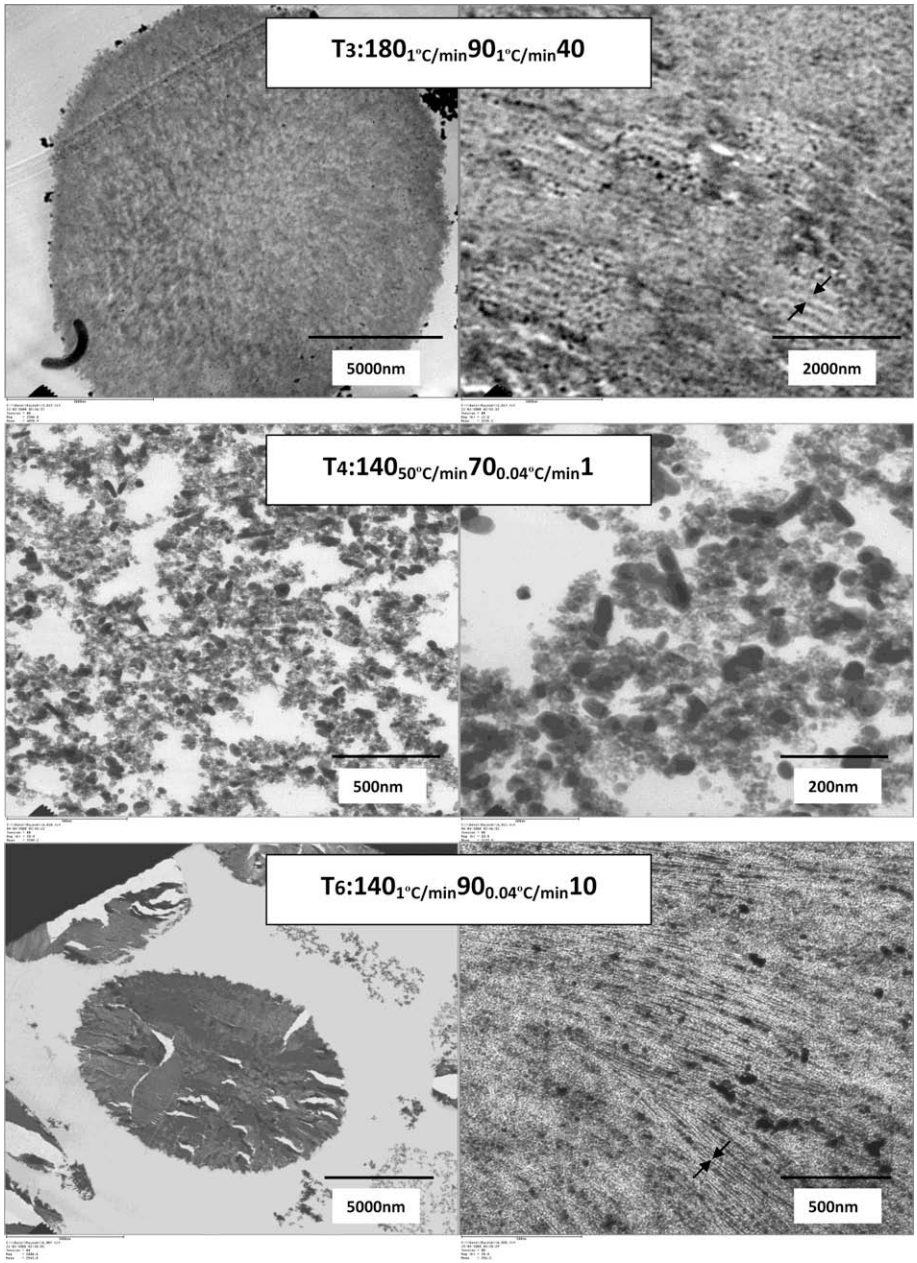

Fig. 5. TEM images of spherulite of amylose–PA for treatment 3, 4 and 6. Scale bar marked on image.

3.6. Enzyme resistance of amylose–PA spherulites

Both added and endogenous lipids have influence on starch digestibility and resistant starch formation (Crowe, Seligman, & Copeland, 2000; Eliasson & Krog, 1985; Gelders et al., 2005; Guraya, Kadan, & Champagne, 1997; Holm et al., 1983; Nebesny, Rosicka, & Tkaczyk, 2002; Szczodrak & Pomeranz, 1991). Complexes with greater crystallinity are more resistant to enzymatic degradation. The rate and extent of degradation by bacterial and pancreatic amylases has been seen to decrease in the order of: Form I > Form IIa > Form IIb (Tufvesson, Wahlgren, & Eliasson, 2003). Resistant starch content for spherulites from the two typical spherulitic morphologies, i.e. spherical and torus (treatment 3 and 6) was 28% and 39%, respectively. The increase in resistant starch content in treatment 6 can be attributed to the presence of crystalline V-complex. Spherulites from treatment 3, despite having mixed (B+V)-type crystallinity were less resistant, probably because the V-amylose was type I and there was a lesser degree of B-type crystallinity.

Optical microscopy of spherulite residue after resistant starch digestion is shown in Fig. 6. Spherical spherulites (treatment 3) maintained their granular structure, while torus-shaped spherulites lost granularity. The morphology of amylose–PA spherulites before and after resistant starch determination was examined using scanning electron microscopy (Fig. 7). Spherical-shaped spherulites are pitted in a manner reminiscent of that observed for the enzymatic degradation of native starch granules (Berry, I'anson, Miles, Morris, & Russell, 1988; Helbert, Schulein, & Henrissat, 1996). Oates (1997) proposed that the degradation pattern of resistant starch occurs in two steps: (1) creation of a superficial microporosity due to uniform adsorption of enzyme molecules, and (2) degradation leading to macroporosity, with deeper grooves where the enzymes encounter a less organized structure. In con-

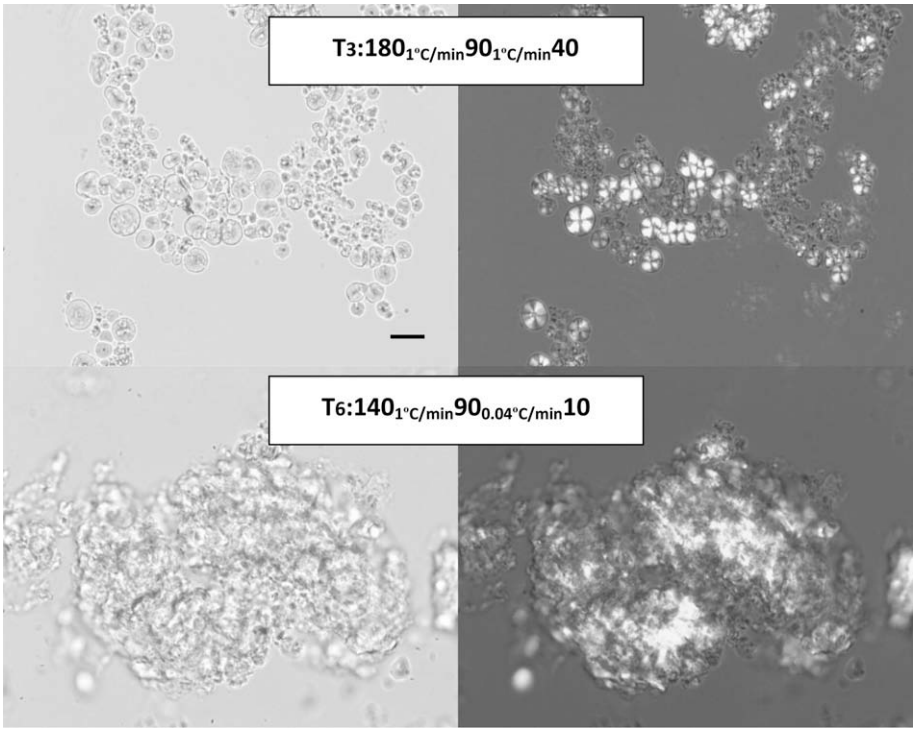

Fig. 6. Optical microscope images under normal and between crossed polarized light of experiments of amylose–PA spherulites after resistant starch digestion process, treatments 3 and 6. Bar equals 20 μm.

trast, the torus-shaped spherulites appear more evenly degraded with evidence of accretion due to recrystallization.

Polymorphic transformation from V- to B-type crystallinity, treatment 6, or mixed V+B to B-type, treatment 3, was observed on enzymatic digestion (Fig. 8). Such transitions have been described earlier for amylose–ethanol complexes and shown to be favored for short chain amylose. The observed transformations were likely due to recrystallization following hydrolysis.

The DSC melting profile of treatment 3 after resistant starch digestion (Fig. 9) shows little qualitative difference from that before digestion (Fig. 4), though shifted to a higher peak temperature, consistent with the previous suggestion that the endotherm in Fig. 4 includes contributions from both V- and B-type crystallites. Melting of digested spherulites from treatment 6 (Fig. 9) clearly shows evidence of recrystallization into the B-polymorph characteristic of retrograded starch.

4. Conclusions

Spherulite morphology and their susceptibility to enzymatic degradation appear to be governed by complex interactions between a number of variables including the endpoint temperature, the quench temperature and the cooling rate. Since we rarely observed mixed morphology, i.e. both spherical and torus-shaped spherulites, in a single sample, it is likely that such mixed morphology observed by Fanta et al. (2008) was due to variations in the thermal profile with position in the Dewar flasks. Therefore, scale-up of the process would require a high degree of control over the temperature, especially the cooling rate. Morphology and degradation pattern would largely determine the suitability of starch spherulites for controlled or targeted release systems, and it appears that they can be selectively tailored by choosing proper experimental conditions, although additional research is needed to fully understand spherulite formation.

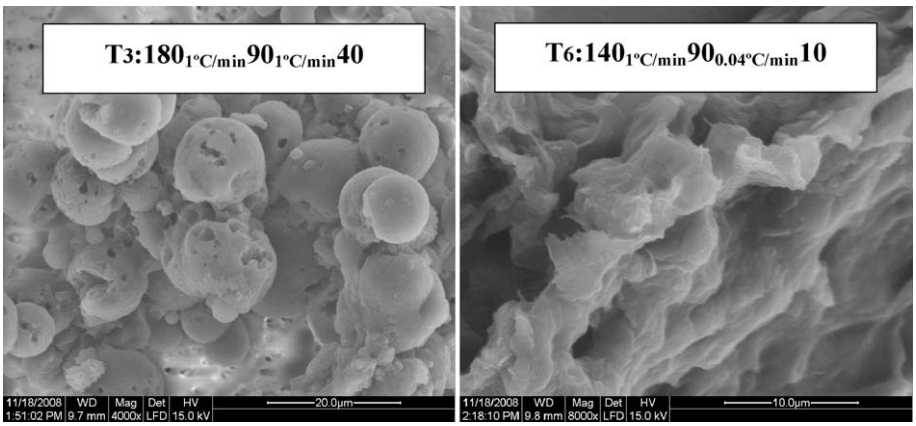

Fig. 7. SEM images of amylose–PA spherulites after resistant starch after digestion process, treatments 3 and 6. Scale bar marked on image.

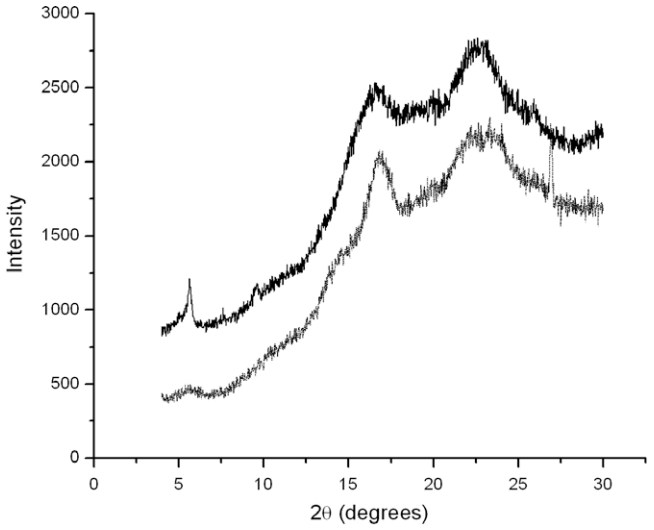

Fig. 8. X-ray diffraction diagrams of amylose–PA spherulites after resistant starch digestion, process, treatments 3 (gray, lower line) and 6 (black, upper line).

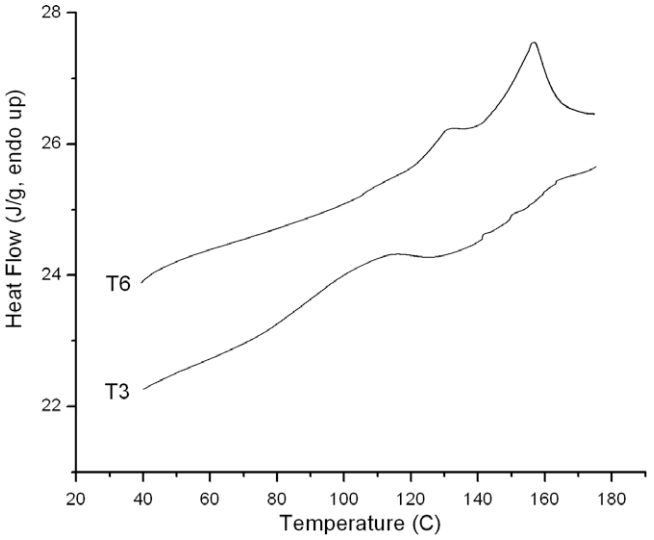

Fig. 9. DSC thermograms of amylose–PA spherulites after resistant starch digestion process, treatments 3 and 6.

References

Berry, C. S., I'anson, K., Miles, M. J., Morris, V. J., & Russell, P. L. (1988). Physical-chemical characterization of resistant starch from wheat. *Journal of Cereal Science, 8*, 203–208.

Biais, B., Le Bail, P., Robert, P., Pontoire, B., & Buleon, A. (2006). Structural and stoichiometric studies of complexes between aroma compounds and amylose. Polymorphic transitions and quantification in amorphous and crystalline areas.. *Carbohydrate Polymers, 66*, 306–315.

Byars, J. A., Fanta, G. F., & Felker, F. C. (2003). The effect of cooling conditions on jet-cooked normal starch dispersions. *Carbohydrate Polymers, 54*, 321–326.

Byars, J. A., Fanta, G. F., & Felker, F. C. (2006). The influence of oil on the properties of slowly-cooled jet-cooked normal corn starch dispersions. *Carbohydrate Polymers, 63*, 316–322.

Conde-Petit, B., Escher, F., & Nuessli, J. (2006). Structural features of starch-flavor complexation in food model systems. *Trends in Food Science & Technology, 17*, 227–235.

Creek, J. A., Benesi, A., Runt, J., & Ziegler, G. R. (2007). Potential sources of error in the calorimetric evaluation of amylose content of starches. *Carbohydrate Polymers, 68*, 365–371.

Creek, J. A., Ziegler, G. R., & Runt, J. P. (2006). Amylose crystallization from concentrated aqueous solution. *Biomacromolecules, 7*, 761–770.

Crowe, T. C., Seligman, S. A., & Copeland, L. (2000). Inhibition of enzymic digestion of amylose by free fatty acids in vitro contributes to resistant starch formation. *Journal of Nutrition, 130*, 2006–2008.

Eliasson, A. C., & Krog, N. (1985). Physical properties of amylose monoglyceride complexes. *Journal of Cereal Science, 3*, 239.

Fanta, G. F., Felker, F. C., & Shogren, R. L. (2002). Formation of crystalline aggregates in slowly-cooled starch solutions prepared by steam jet cooking. *Carbohydrate Polymers, 48*, 161–170.

Fanta, G. F., Felker, F. C., Shogren, R. L., Byars, J. A., & Salch, J. H. (2005). Crystalline particles formed in slowly-cooled cornstarch dispersions prepared by steam jet cooking: The effect of starch concentration, added oil and rate of cooling. *Carbohydrate Polymers, 61*, 222–230.

Fanta, G. F., Felker, F. C., Shogren, R. L., & Salch, J. H. (2006). Effect of fatty acid structure on the morphology of spherulites formed from jet cooked mixtures of fatty acids and defatted cornstarch. *Carbohydrate Polymers, 66*, 60–70.

Fanta, G. F., Felker, F. C., Shogren, R. L., & Salch, J. (2008). Preparation of spherulites from jet cooked mixtures of high amylose starch and fatty acids: Effect of preparative conditions on spherulite morphology and yield. *Carbohydrate Polymers, 71*, 253–262.

Fanta, G. F., Shogren, R. L., & Salch, J. H. (1999). Steam jet cooking of high amylose starch–fatty acid mixtures: An investigation of complex formation. *Carbohydrate Polymers, 38*, 1–6.

Felker, F. C., & Fanta, G. F. (2006). Selective formation and yield enchancement of spherulites in jet-cooked nigh-amylose cornstarch dispersions. *Whole grain summit: Foods and beverages 2006*. San Francisco, CA [Abstract P-314]. http://www.wgsummit.org/program/pdfs/OralsPostersOnly.pdf. Accessed 29.06.2009.

Gallant, D. J., Mercier, C., & Guilbot, A. (1972). Electron microscopy of starch granules modified by bacterial alpha amylase. *Cereal Chemistry, 49*, 354–365.

Gelders, G. G., Duyck, J. P., Goesaert, H., & Delcour, J. A. (2005). Enzyme and acid resistance of amylose–lipid complexes differing in amylose chain length, lipid and complexation temperature. *Carbohydrate Polymers, 60*, 379–389.

Godet, M. C., Bizot, H., & Buléon, A. (1995). Crystalization of amylose–fatty acid complexes prepared with different amylose chain lengths. *Carbohydrate Polymers, 27*, 47–52.

Godet, M. C., Bouchet, B., Colonna, P., Gallant, D. J., & Buléon, A. (1996). Crystalline amylose–fatty acid complexes: Morphology and crystal thickness. *Journal of Food Science, 61*(6), 1196–1201.

Guraya, H. S., Kadan, R. S., & Champagne, E. T. (1997). Effect of rice starch–lipid complexes on in vitro digestibility, complexing index, and viscosity. *Cereal Chemistry, 74*, 561–565.

Heinemann, C., Escher, F., & Conde-Petit, B. (2003). Structural features of starch-lactone inclusion complexes in aqueous potato starch dispersions: The role of amylose and amylopectin. *Carbohydrate Polymers, 51*, 159–168.

Helbert, W., Schulein, M., & Henrissat, B. (1996). Electron microscopic investigation of the diffusion of *Bacillus licheniformis* alpha-amylase into corn starch granules. *International Journal of Biological Macromolecules, 19*, 165–169.

Holm, J., Bjorck, I., Ostrovska, S., Eliasson, A. C., Asp, N. G., Larsson, K., et al. (1983). Digestibility of amylose–lipid complexes in vitro and in vivo. *Starch/Stärke, 35*, 294–297.

Karkalas, J., Ma, S., Morrison, W., & Pethrick, R. A. (1995). Some factors determining the thermal properties of amylose inclusion complexes with fatty acids. *Carbohydrate Research, 268*, 233–247.

Kim, J. Y., & Lim, S. T. (2009). Preparation of nano-sized starch particles by complex formation with *n*-butanol. *Carbohydrate Polymers, 76*, 110–116.

Kim, J. Y., Yoon, J. W., & Lim, S. T. (2009). Formation and isolation of nanocrystal complexes between dextrins and *n*-butanol. *Carbohydrate Polymers*. doi:10.1016/j.carbpol.2009.05.026.

McCleary, B. V., McNally, M., & Rossiter, P. (2002). Measurement of resistant starch by enzymatic digestion in starch and selected plant materials: Collaborative study. *Journal of AOAC International, 85*, 1103–1111.

Nebesny, E., Rosicka, J., & Tkaczyk, M. (2002). Effect of enzymic hydrolysis of wheat starch on amylose lipid complexes stability. *Starch/Stärke, 54*, 603–608.

Nordmark, T. S., & Ziegler, G. R. (2002a). Spherulitic crystallization of gelatinized maize starch and its fractions. *Carbohydrate Polymers, 49*, 439–448.

Nordmark, T. S., & Ziegler, G. R. (2002b). Structural features of non-granular spherulitic maize starch. *Carbohydrate Research, 16*(337), 1467–1475.

Oates, C. G. (1997). Towards an understanding of starch granule structure and hydrolysis. *Trends Food Science Technology, 8*, 375–382.

Peterson, S. C., Fanta, G. F., Adlof, R. O., & Felker, F. C. (2005). Identification of complexed native lipids in crystalline aggregates formed from jet cooked cornstarch. *Carbohydrate Polymers, 61*, 162–167.

Shogren, R. L., Fanta, G. F., & Felker, F. C. (2006). X-ray diffraction study of crystal transformations in spherulitic amylose/lipid complexes from jet-cooked starch. *Carbohydrate Polymers, 64*, 444–451.

Sievert, D., & Holm, J. (1993). Determination of amylose with differential scanning calorimetry. *Starch/Starke, 45*, 136–139.

Szczodrak, J., & Pomeranz, Y. (1991). Starch and enzyme-resistant starch from high-amylose barley. *Cereal chemistry, 68*, 589–596.

Tufvesson, F., Wahlgren, M., & Eliasson, A. C. (2003). Formation of amylose–lipid complexes and effects of temperature treatment. Part 2 fatty acids. *Starch/Stärke, 55*, 138–149.

Whittam, M. A., Orford, P. D., Ring, S. G., Clark, S. A., Parker, M. L., Cairns, P., et al. (1989). Aqueous dissolution of crystalline and amorphous amylose–alcohol complexes. *International Journal of Biological Macromolecules, 11*, 339–344.

Ziegler, G. R., Creek, J. A., & Runt, J. (2005). Spherulitic crystallization in starch as a model for starch granule initiation. *Biomacromolecules, 6*, 1547–1554.

Ziegler, G. R., Nordmark, T. S., & Woodling, S. E. (2003). Spherulitic crystallization of starch: Influence of botanical origin and extent of thermal treatment. *Food Hydrocolloids, 17*, 487–494.